Supplementary Information

An ultra-small, multi-point, and multi-color photo-detection system with high sensitivity and high dynamic range

Takashi Anazawa*[1] and Motohiro Yamazaki[2]

[1]Hitachi, Ltd., Research & Development Group, Japan

[2]Hitachi High-Technologies Corporation, Science & Medical Systems Business Group, Japan

Intensity profile and size of emission-point image

As shown in Figures S1a and S1b, when the same lens (f = 1.44 mm) was used with the emission-point distance (distance between the lens and the emission point) of g = 1.57 mm, normalized intensity profiles of the images of the emission point (dp = 0.05 mm) at the sensor distance (optical length between the lens and the image-sensor surface) of h = 9.7 mm (green line), 11.8 mm (yellow line), 14.3 mm (orange line), and 16.8 mm (red line) were calculated by the ray-trace simulations with one-half light-emission angles of 21° and 10°, respectively. In each figure, not only image diameter but also intensity profile changes with sensor distance. As described in the main text, image diameters (full-width at 10% maximum) are ds = 0.57, 0.53, 0.51, and 0.64 mm in Figure S1a, and ds = 0.42, 0.46, 0.50, and 0.55 mm in Figure S1b, at sensor distances of h = 9.7, 11.8, 14.3, and 16.8 mm, respectively. Image diameter slightly increases with one-half light-emission angle at each sensor distance due to aberrations by a marginal part of the lens. The intensity profile at h = 16.8 mm (red line) is rectangular shaped in Figure S1b because the emission point is just in focus with minimal aberrations, whereas it spreads toward the bottom in Figure S1a. The intensity profile at h = 9.7 (green line), 11.8 (yellow line), and 14.3 mm (orange line) in Figure S1b is a trapezoid or triangle shaped because the emission point is somewhat out of focus.

Normalized intensity profiles of images S_{11}, S_{12}, S_{13}, and S_{14} in Figure 4f are shown in Figure S1c by green, yellow, orange, and red lines, respectively. The intensity profiles are consistent with those in Figure S1b. Other intensity profiles of images S_{i1}, S_{i2}, S_{i3}, and S_{i4} where i = 2, 3, and 4 in Figure 4f are also consistent with those in Figure S1b. As described in the main text, image diameters (full-width at 10% maximum) of S_{i1}, S_{i2}, S_{i3}, and S_{i4} in Figure 4f are ds_1 = 0.40 ± 0.01 mm, ds_2 = 0.45 ± 0.01 mm, ds_3 = 0.48 ± 0.01 mm, and ds_4 = 0.54 ± 0.01 mm (average ± standard deviation for i = 1, 2, 3, and 4).

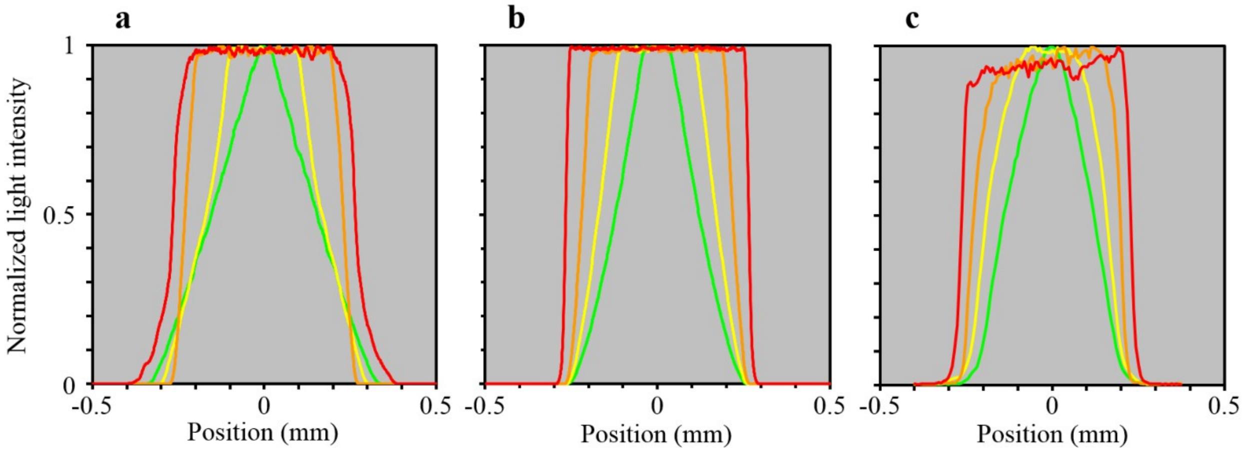

Figure S1

Influence of emission-point distance on size of emission-point image

When the same lens (f = 1.44 mm) was used, image diameter ds (full-width at 10% maximum) of the emission point (dp = 0.05 mm and one-half light-emission angle of 10°) was calculated as a function of sensor distance h (optical length between the lens and the image-sensor surface) and emission-point distance g (distance between the lens and the emission point) by the light-ray-trace simulations and is shown in Figure S2. Figure S2b is an enlarged graph of Figure S2a. When $g = f$ = 1.44 mm (black plots and line), that is, the emission point is at the focal point of the lens, light from the emission point is collimated, and ds is smallest at infinity (for example, at h= 100 mm), as shown in Figure S1a. Here, ds increases with h, because the emission-point size is finite (dp = 0.05 mm); therefore, the flux formed by the lens is not perfectly parallel. On the other hand, under the condition in Figure S1b, namely, g = 1.57 mm (sky blue plots and line), ds_4 is smallest because, as indicated by Equation (1), the emission point is focused at $h = h_4$ = 16.8 mm. Similarly, when g = 1.60 mm (green plots and line), 1.63 mm (orange plots and line), and 1.68 mm (red plots and line), that is, the emission point is focused at $h = h_3$ = 14.3, h_2 = 11.8, and h_1 = 9.7 mm, respectively, as indicated by Equation (1), ds_3, ds_2, and ds_1 are smallest, respectively. Moreover, under these conditions, ds increases with h when $h > h_1$ = 9.7 mm (i.e., $ds_1 < ds_2 < ds_3 < ds_4$) as also shown in Figures S1b and S1c. It is therefore concluded that ds at $h_1 < h < h_4$ is minimized (i.e., ds_4 (maximum of ds_1, ds_2, ds_3, and ds_4) is minimized) when the emission point is focused at $h = h_4$. In general, ds at $h_1 < h < h_j$ is minimized (i.e., ds_j (maximum of ds_1, $\cdots$, ds_j) is minimized) when the emission point is focused at $h = h_j$.

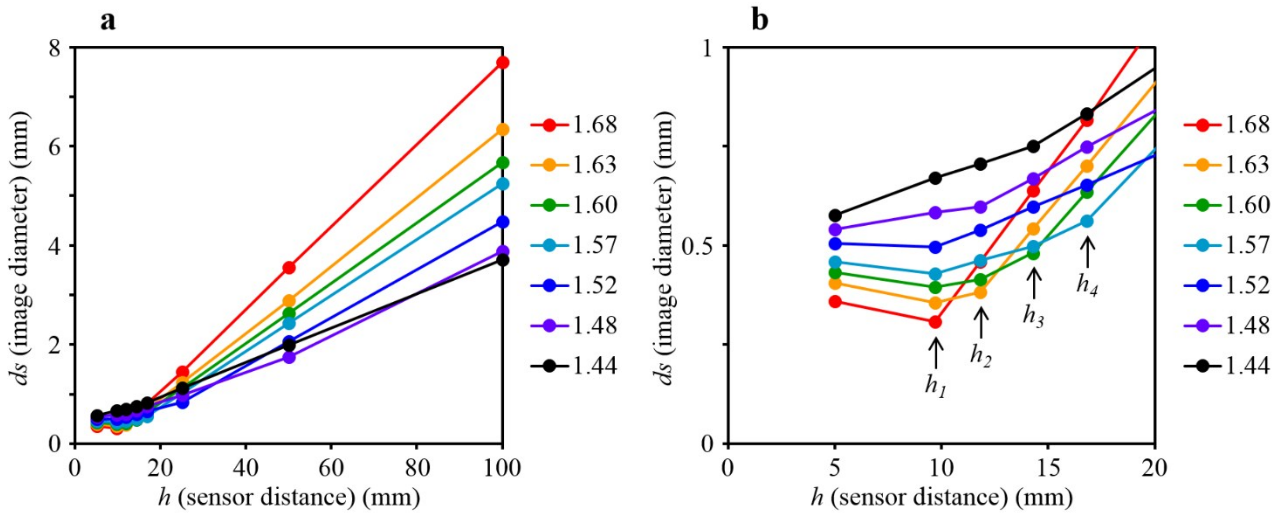

Figure S2

Four-capillary-array detection system

The ultra-small, four-capillary-array, and four-color-fluorescence-detection system is shown in Figure 3S, where the system in Figure 2a is connected by the four-capillary array with the laser beam as shown in Figure 5. As described in the main text, the detection points (D_i) of the capillaries (P_i) are positioned at the emission points (E_i) in Figure 2a so that axes of the capillaries are perpendicular to the array directions of the four emission points and the four lenses and parallel to the sensor surface. The laser beam (with the diameter of 0.01 mm) enters the side of the capillary-array plane and then simultaneously irradiates the detection points of the capillaries (with the inner-diameters of 0.05 mm). Therefore, rectangular-shaped emission points with widths of dp = 0.05 mm and heights of 0.01 mm are formed. Ray-trace simulation results of rays emitted from the emission points and collected by the lenses are overlaid in Figure 3S, where one-half light-emission angles from the emission points are 21°. Whereas sixteen circular images are shown in Figure 2a, sixteen rectangular images of the four emission points are shown on the sensor surface. Any two of the rectangular images do not overlap; that is, low-crosstalk fluorescence detection is achieved. These results are consistent with those shown in Figure 6.

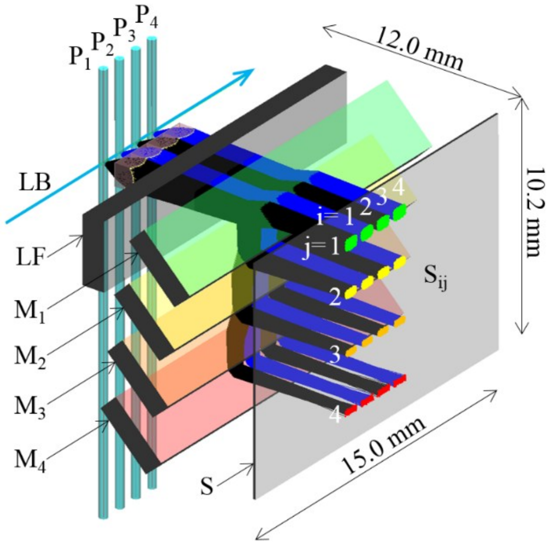

Figure 3S

Dichroic-mirror arrays in stepwise and non-stepwise manners

As shown in Figure 2b, the four dichroic mirrors are arrayed in a stepwise manner at intervals of 2.5 mm not only to miniaturize the system but also to widen aperture W of the system. In Figure S4a, step differences between dichroic mirrors are added to Figure 2b; step difference between M_1 and M_2 is 0.7 mm, and step differences between M_2 and M_3, and M_3 and M_4 are both 0.3 mm. On the other hand, as shown in Figure S4b, when the four dichroic mirrors are arrayed in a non-stepwise manner at intervals of 2.5 mm, that is, step differences between dichroic mirrors are all zero, W is considerably decreased from 1.4 to 0.03 mm due to vignetting in the four-dichroic-mirror array. Even when arrayed in the non-stepwise manner, the thinner dichroic mirrors enable larger W because parallel displacements of the fluxes in the dichroic mirrors are reduced. However, it is difficult to manufacture such dichroic mirrors with thicknesses of less than 1 mm, because warpage of the dichroic-mirror surfaces is brought about during the manufacturing process. It is therefore concluded that it is necessary to array the dichroic mirrors in a stepwise manner to achieve a miniaturized and highly sensitive system.

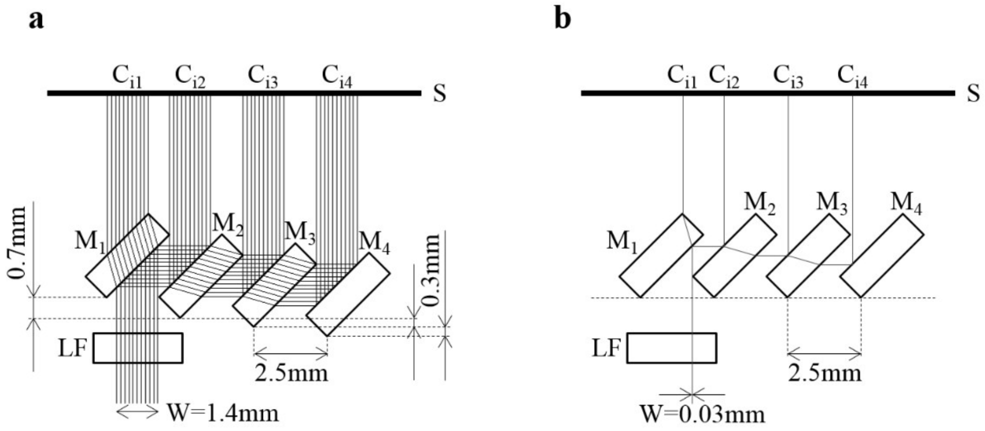

Figure S4

Transmission spectra of longpass filter and dichroic mirrors

Measured transmission spectrum of the fabricated *LF* at incident angle of 0° and measured transmission spectra of the fabricated M_1, M_2, M_3, and M_4 at incident angle of 45° are shown in Figure S5 and indicated by black, green, yellow, orange, and red lines, respectively. Each *LF* and M_j meets the below specification, where *IA*, *T*, T_{ave}, and *R* are incident angle, transmittance, averaged transmittance, and reflectance for unpolarized light.

LF: $IA = 0°$, $T \leq 0.01\%$ at 505 nm, $T_{ave} \geq 95\%$ at 530−650 nm, and $T \geq 90\%$ at 530−650 nm

M_1: $IA = 45°$, $T_{ave} \geq 90\%$ at 530−545 nm, and $R \geq 95\%$ at 565−650 nm

M_2: $IA = 45°$, $R \geq 95\%$ at 560−575 nm and $T_{ave} \geq 90\%$ at 595−650 nm

M_3: $IA = 45°$, $R \geq 95\%$ at 590−605 nm and $T_{ave} \geq 90\%$ at 625−650 nm

M_4: $IA = 45°$, $R \geq 95\%$ at 615−650 nm

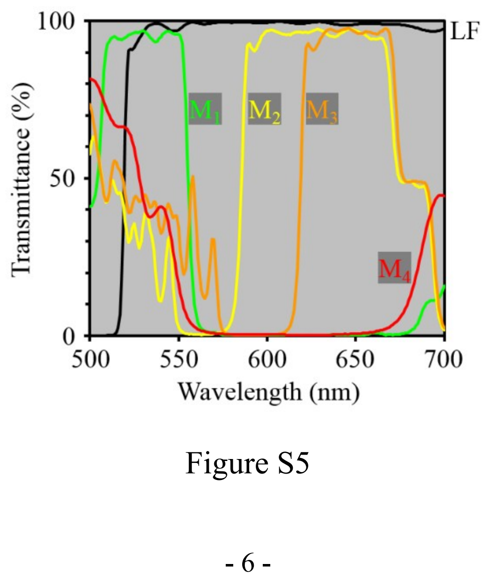

Figure S5